Water Utility Journal (2026) 35:1

Evaluation of a depth-averaged numerical model for self-aerated open channel flows

Y.T. Zerihun

David & James - Engineering and Environmental Consultancy, 204 Albion Road, Victoria 3350, Australia
e-mail: zyebegaeshet@gmail.com

Abstract: For several decades, physical model tests have been extensively employed to investigate the important features of self-aerated flow in an open channel. The results of such tests, however, have limitations to their applicability, depending on the scope of the tests on which they are based. Herein, a mixture flow model, which incorporates a coupled set of depth-averaged Boussinesq-type and air transport equations, was developed and applied to analyze the problems of self-aerated flow. These governing equations were discretized and solved by a hybrid scheme that applies the finite-volume and finite-difference methods. The credibility of the proposed model for solving such types of turbulent flow problems was examined using results from the experiments. A quite satisfactory agreement was found. Despite the complex three-dimensional character of the flow, the dynamic behavior of air-water interactions was favorably captured. Overall, the results of this study confirm the model's validity in predicting the mean flow features of the self-aerated flow.

Key words: Air-water flow; bubble transport; finite-volume method; hypercritical flow; mixture flow model; self-aeration.

1. INTRODUCTION

High-velocity flows in open channels are normally aerated at the free surface, transforming incompressible clear-water flows into compressible air-water mixture flows. A typical example of aerated flow is an open-channel bubbly flow, where air is entrained and carried along with the water in the form of bubbles of different sizes (Wilhelms and Gulliver, 2005). Flow aeration may cause bulking of flow (Hall, 1943; Falvey, 1980) and reduction of flow resistance (Jevdjevich and Levin, 1953; Wood, 1983). As noted by Killen (1968), the existence of air bubbles does not change the typical velocity distribution of a supercritical open-channel flow. In engineering practice, self-aerated flows are commonly encountered along the spillway chute and an energy dissipator (refer to Figure 1). Given the large computational domains involved in analyzing the problems of flows over such structures, the application of eddy resolving modeling techniques is not viable. Consequently, a numerical simulation approach based on the Reynolds-averaged Navier-Stokes (RANS) equations is commonly applied to aid in the design of these types of river infrastructures. Such higher-order equations can capture the realistic flow behavior of two-dimensional (2D) and three-dimensional (3D) problems of air-water flows. In this study, the depth-averaged RANS equations are integrated with an air entrainment module to develop a non-hydrostatic two-phase flow model.

The flow fields of self-aerated open-channel flow have been experimentally studied by numerous investigators. Straub and Anderson (1960) systematically investigated the salient features of the aerated supercritical flow in the uniform flow region of an artificially roughened chute. They also examined the shape of the air concentration distribution at a vertical section. Since then, several studies explored the turbulent characteristics of the aerated flow including the turbulence intensities, the bubbly two-phase flow regime, and the structure of the flow field (e.g., Killen, 1968; Chanson and Toombes, 2002; Boes and Hager, 2003a; Ohtsu et al., 2004; Wilhelms and Gulliver, 2005; Kramer et al., 2006; Felder and Chanson, 2009; Pfister and Hager, 2011; Estrella et al., 2022). Besides, Wood (1983) and Hager (1991) analyzed the experimental data obtained by Straub and

Anderson; they proposed empirical equations to predict the air concentration in the uniform aerated flow zone. All these experimental studies shed light on the understanding of the physical processes of air-water flows.

Figure 1. Aerated flows in hydraulic structures: (a) flow over the emergency spillway of the Grand Ethiopian Renaissance Dam; and (b) water jets from the spillway of the Gibe III Dam, Ethiopia (Photographs courtesy of Studio Pietrangeli Consulting Engineers, Italy).

A computational model capable of accurately predicting the 2D characteristics of air-water flow plays a vital role for developing a strategy to prevent the potential of cavitation erosion. Over the past few years, several types of two-phase flow models have been developed to solve the turbulent mixture flow problems. The hydrodynamic part of these models adopts the RANS equations together with a mixture flow or a two-fluid flow modeling approach. As discussed by Ishii and Hibiki (2011, p. 155), the latter approach is more complicated than the former one in terms of the number of field equations involved. Yan and Che (2010) presented a model for analyzing two-phase flow problems, in which both small and large length scale interfaces are coexisted. They proposed a numerical treatment based on the volume fraction redistribution approach to deal with the complex flow problems. By considering the local turbulent kinetic energy near the interface and the velocity gradient normal to the free surface, Ma et al. (2011) introduced a sub-grid air entrainment module and coupled it with the Reynolds averaged two-fluid equations. The accuracy of the proposed model was tested by simulating plunging jets and hydraulic jumps, resulting in a good agreement with the experimental results. An air entrainment module, which relies on the interaction of vortices with a free surface, was also introduced by Castro et al. (2016). They applied a linear superposition method to evaluate the total rate of air entrainment from the contributions of each vortex. Using an analogous mathematical approach to Ma et al., Lopes et al. (2017) proposed a sub-grid module based on an advection-diffusion equation and implemented it into the OpenFOAM software. For aerated flow over a stepped spillway, they examined the model's performance and obtained a satisfactory result. However, the effectiveness of such types of numerical models is largely determined by the method used for coupling the bubble transport module with the interface capturing technique for the free surface. Based on the balance of the effects of turbulence, gravity, and surface tension, an air entrainment module was also developed and incorporated into the FLOW-3D software (Hirt, 2003; Souders and Hirt, 2004). Recently, this software package was used to analyze different types of self-aerated flow problems (e.g., Valero and García-Bartual, 2016; Morovati and Eghbalzadeh, 2018). Under the framework of the RANS equations, Zabaleta et al. (2023) proposed a numerical model for analyzing such types of flow problems. A three-phase mixture approach made of a continuous air, bubble, and water phases was adopted by this model. For engineering problems with an extensive computational domain, however, it is computationally intensive to compute the local aerated flow parameters and variations of free-surface profile using the aforesaid models. Consequently, many numerical studies (e.g., Olsen and Kjellesvig, 1998; Chanel and Doering, 2008; Kirkgoz et al., 2009; Ho and Riddette, 2010) aimed to merely examine the global flow characteristics of single-phase flows over spillway chutes. In contrast, few studies considered the effects of air entrainment when analyzing the dynamic characteristics of chute flows (Valero and García-Bartual, 2016; Almeland et al., 2021; Hohermuth et al., 2021). Despite the numerous experimental investigations conducted, little attention has been paid to studying turbulent aerated flow using a RANS equations-based model. As far as the author is aware, a non-hydrostatic depth-averaged mixture flow model has not been previously introduced to simulate the mean flow characteristics of this type of plane open-channel flow.

In light of the aforementioned reasons, it appears that there is a need to develop a general-purpose numerical model for systematically investigating the problems of self-aerated open-channel flow by treating the flow as a homogeneous water-bubble mixture flow up to a depth at which the air concentration reaches 90%. Therefore, this study primarily aims at developing a non-hydrostatic mixture flow model by coupling the depth-averaged Boussinesq-type equations (Zerihun, 2024) with a depth-averaged air transport equation. The equation governing air transport includes a source term to assess the self-aeration process. Such a mixture flow model has the capacity to predict the mean and bottom air concentrations as well as the local flow characteristics, and it obviates the drawbacks of the existing higher-order, depth-averaged models for single-phase flows. These models under-predict the axial free-surface profile of a free hydraulic jump partly due to the absence of a correction factor that accounts for the effects of flow bulking (Zerihun, 2021). Compared to a 3D or a computational fluid dynamics model, it is considerably easier to implement and needs much less computational efforts to obtain converged solutions after calibration, thus making it as a preferable design tool for developing or modifying the conceptual design of an energy dissipator or a smooth spillway. It is also aimed at conducting numerical tests to examine the effects of air entrainment on the local flow characteristics and to evaluate the model's validity for self-aerated flow problems. It is worth emphasizing that the bubble breakup and coalescence processes are not considered in this study. These competing processes directly affect the results of the mean air concentration for a highly turbulent flow. Consideration of the resulting minor errors is however ignored. The following sections will provide concise overviews of the formulation of the governing equations and the numerical solution procedures, along with an in-depth description of the validations of the model results with the measurements.

2. DEPTH-AVERAGED MATHEMATICAL MODEL

2.1 Governing equations

A 2D open-channel, air-water flow over a rigid bed is considered, as depicted in Figure 2. A Cartesian coordinate system, with the x-axis in the main downstream direction, y-axis in the transverse direction, and the z-axis oriented vertically, is also shown in this figure. For two-phase flow in a rectangular channel, the modified version of the depth-averaged Boussinesq-type equations (Zerihun, 2024) reads as follows:

$$\frac{\partial H}{\partial t}+\frac{\partial q}{\partial x}=-\frac{1}{\rho}\left(q\frac{\partial \rho}{\partial x}+H\frac{\partial \rho}{\partial t}\right), \tag{1}$$

$$\frac{\partial}{\partial t}(\rho q)+\frac{\partial}{\partial x}\left(\frac{\rho q^2}{H}\beta_1+\frac{\rho g H^2}{2}\right)-\frac{\partial}{\partial x}\left(H\overline{\sigma}_x\right)+\left(\rho g H+p_D\right)\frac{\partial Z}{\partial x}+\frac{\partial}{\partial x}\left(\frac{Hp_D}{2}\right)+\tau_b=0, \tag{2}$$

$$\frac{\partial}{\partial t}\left(\rho\beta_4 q\frac{\partial H}{\partial x}+\rho\beta_3 H\frac{\partial H}{\partial t}\right)+\frac{\partial}{\partial x}\left(\rho\left(\frac{q^2}{H}\left(\beta_2\frac{\partial H}{\partial x}+\beta_1\frac{\partial Z}{\partial x}\right)\right)+\frac{q\rho}{2}\frac{\partial H}{\partial t}\right)$$
$$-\frac{\partial}{\partial x}\left(H\bar{\tau}_{zx}\right)-p_D+\tau_b\frac{\partial Z}{\partial x}=0, \tag{3}$$

where τ_b is the bed shear stress; $\bar{\sigma}_x$ and $\bar{\tau}_{zx}$ are the depth-averaged normal and tangential stresses, respectively; q is the unit discharge; H is the mixture flow depth; Z is the channel bed elevation; g is acceleration due to gravity; ρ is the density of the air-water mixture; t is the time; p_D is the dynamic pressure at the channel bed; $\beta_1=\left(\omega^2-2\omega+4\right)/3$; $\beta_2=\left(\omega^2-4\omega+6\right)/6$; $\beta_3=\left(\omega+2\right)/6$; and $\beta_4=\left(4-\omega\right)/6$. The turbulent stresses appearing in the preceding equations are evaluated using a depth-averaged turbulence closure model. This model will be presented in the following section.

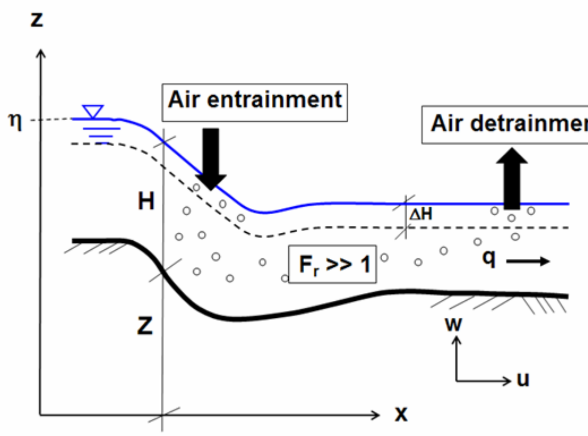

Figure 2. Schematic representation of turbulent, air-water open-channel flow. F_r stands for the Froude number of the flow.

The distributions of the Cartesian velocity components across the flow depth are described by the following equations:

$$u=\frac{q}{H}\left(2\Lambda(1-\omega)+\omega\right), \tag{4a}$$

$$w=\frac{\partial H}{\partial t}\left(1-\omega(1-\Lambda)-(1-\omega)\left(1-\Lambda^2\right)\right)+\frac{q}{H}\frac{\partial\eta}{\partial x}(2-\omega)-\frac{2q}{H}\frac{\partial Z}{\partial x}\left((1-\omega)(1-\Lambda)\right)$$
$$-\frac{q}{H}\frac{\partial H}{\partial x}\left((1-\Lambda)\omega\right)-\frac{2q}{H}\frac{\partial H}{\partial x}\left((1-\omega)\left(1-\Lambda^2\right)\right), \tag{4b}$$

$$\Lambda=\frac{z-Z}{\eta-Z}, \tag{4c}$$

where u and w are the velocity components in the x- and z-directions, respectively; ω is a velocity distribution parameter; Λ is a dimensionless vertical coordinate; z is the vertical elevation of a point in the flow field; and η is the free-surface elevation.

The density of the mixture flow may vary along the flow direction, but it is presumed to be constant at a section. Based on volumetric concentration, it is expressed as

$$\rho = \rho_w(1 - C_m) + \rho_a C_m, \tag{5}$$

where the subscripts w and a stand for water and air, respectively, and C_m is the mean air concentration. In the proposed model, the effect of air transport phenomenon is considered by using the density and dynamic viscosity of the mixture flow. The bed shear stress is determined by the Gauckler–Manning equation as follows:

$$\frac{\tau_b}{\rho} = \frac{g n_m^2 q^2}{R_H^{1/3} H^2}\left(1 + \left(\frac{\partial Z}{\partial x}\right)^2\right), \tag{6}$$

where n_m is the Gauckler–Manning roughness coefficient, and R_H is the hydraulic radius with the wetted perimeter evaluated based on a cross-sectional plane normal to the bed. As described before, self-aeration causes flow resistance reduction which can be estimated by an empirical equation (Chanson, 1994; Boes and Hager, 2003b).

The pressure distribution at a vertical section is given by

$$p = (\rho g H + p_D)(1 - \Lambda), \tag{7}$$

where p is the sum of the static and dynamic pressure components. Similar to the equations of Zerihun (2016), the proposed equations incorporate the effects of the steep slope of a channel. It is important to highlight that the proposed depth-averaged model provides approximate solutions to the 3D mixture flow problems by ignoring the effects of the variations of the parameters in the transverse direction. Consequently, the mean free-surface and bed pressure profiles along the centerline of the channel, as well as the local flow characteristics at various sections of the channel, can be simulated.

2.2 Turbulence closure model

Using the Boussinesq (1877) equation, the following expressions for the depth-averaged normal and tangential stresses are obtained by ignoring the effects of air concentration:

$$H\bar{\sigma}_x = 2(\mu + \bar{\xi})\left(\frac{\partial q}{\partial x} - \frac{q}{H}(2-\omega)\frac{\partial \eta}{\partial x}\right) - \frac{2}{3}\rho H \bar{k}, \tag{8}$$

$$H\bar{\tau}_{zx} = (\mu + \bar{\xi})\left(\frac{\partial}{\partial x}\left(q\left(\beta_4 \frac{\partial H}{\partial x} + \frac{\partial Z}{\partial x}\right) + \beta_3 H \frac{\partial H}{\partial t}\right) + \left(\frac{q}{H}(2-\omega)\frac{\partial \eta}{\partial x}\right)\right), \tag{9}$$

where $\bar{\xi}$ and $\bar{k}$ are the depth-averaged eddy viscosity and turbulent kinetic energy, respectively, and μ is the molecular dynamic viscosity of the mixture flow. These expressions for the turbulent stresses are numerically combined with the governing equations. Numerous turbulence models for analyzing open-channel flow are introduced in the past. Here, the depth-averaged form of the standard $k-\varepsilon$ turbulence model (Jones and Launder, 1972) is applied. In this model, the eddy viscosity is reckoned from the following expression:

$$\bar{\xi} = \rho \frac{C_\mu \bar{k}^2}{\bar{\varepsilon}}, \tag{10}$$

where $C_\mu = 0.09$, and $\bar{\varepsilon}$ is the turbulent kinetic energy dissipation rate. For complex aerated flows, the depth-averaged turbulence closure model balances the need for accurate prediction of the variation of the turbulence intensity field with computational efficiency. Additionally, it can approximate the anisotropic turbulence condition by relating Reynolds stresses to mean velocity gradients using average values of relevant flow parameters.

The turbulence variables are determined by modifying the depth-averaged $k-\varepsilon$ turbulence model of Rastogi and Rodi (1978) for a 2D flow problem in the vertical plane. The resulting expressions are as follows:

$$\frac{\partial}{\partial t}\left(\rho H\bar{k}\right)+\frac{\partial}{\partial x}\left(\rho H\bar{U}\bar{k}\right)-\frac{\partial}{\partial x}\left(\left(\mu+\frac{\bar{\xi}}{\sigma_k}\right)H\frac{\partial\bar{k}}{\partial x}\right)-\rho H\left(P_H\frac{\bar{k}^2}{\bar{\varepsilon}}+P_{k\xi}-\bar{\varepsilon}\right)=0, \tag{11a}$$

$$\frac{\partial}{\partial t}\left(\rho H\bar{\varepsilon}\right)+\frac{\partial}{\partial x}\left(\rho H\bar{U}\bar{\varepsilon}\right)-\frac{\partial}{\partial x}\left(\left(\mu+\frac{\bar{\xi}}{\sigma_\varepsilon}\right)H\frac{\partial\bar{\varepsilon}}{\partial x}\right)-\rho H\left(C_{1\varepsilon}\bar{k}P_H+P_{\varepsilon\xi}-C_{2\varepsilon}\frac{\bar{\varepsilon}^2}{\bar{k}}\right)=0, \tag{11b}$$

$$P_H = 2C_\mu\left(\frac{\partial\bar{U}}{\partial x}\right)^2, \tag{11c}$$

$$P_{k\xi}=\frac{U_\tau^3}{H\sqrt{C_f}}, \tag{11d}$$

$$P_{\varepsilon\xi}=\frac{3.6C_{2\varepsilon}U_\tau^4C_\mu^{1/2}}{H^2C_f^{3/4}}, \tag{11e}$$

$$U_\tau=\sqrt{\frac{\tau_b}{\rho}}, \tag{11f}$$

$$\mu=\mu_w\left(1-C_m\right)+\mu_aC_m, \tag{11g}$$

where U_τ is the boundary shear velocity; $C_f = gn_m^2/H^{1/3}$; and $\bar{U}(=q/H)$ is the depth-averaged horizontal velocity. The standard values of the closure coefficients are: $C_{1\varepsilon}=1.44$; $C_{2\varepsilon}=1.92$; $\sigma_k=1.0$; and $\sigma_\varepsilon=1.30$. For completely solving the problems of turbulent flow with air entrainment, Equations (8)-(11g) are combined with Equations (2) and (3).

2.3 Equations for modeling entrainment of air

2.3.1 Air transport equation

The temporal and spatial variability of air concentration is governed by the advection-diffusion equation. In comparison with the z-direction diffusive transport, the diffusive transport in the x-direction is small and can be ignored. For a 2D vertical plane flow, the air transport equation reads as (Ishii and Hibiki, 2011, p. 103)

$$\frac{\partial c}{\partial t}+\frac{\partial}{\partial x}(uc)+\frac{\partial}{\partial z}(wc)+\frac{\partial}{\partial z}(w_B c)-\frac{\partial}{\partial z}\left(\xi_a\frac{\partial c}{\partial z}\right)-R_s=0, \tag{12}$$

where c is the air concentration; w_B is the bubble rise velocity in the z-direction; and R_s is the source or sink term. The vertical air bubble diffusion coefficient, denoted as ξ_a, is approximated by the following depth-averaged eddy-viscosity coefficient equation:

$$\xi_a=\zeta K U_\tau H, \tag{13}$$

where $\zeta=1/6$, and K is the von Kármán constant. By performing vertical integration and applying the Leibnitz integral rule and kinematic boundary conditions, the following depth-averaged air transport equation is obtained from Equation (12) assuming a constant air density:

$$\frac{\partial}{\partial t}(HC_m)+\frac{\partial}{\partial x}(qC_m)+\Gamma_1\overline{w}_B C_m-\xi_a\frac{\Gamma_2 C_m}{H}-H\overline{R}_s=0, \tag{14}$$

where Γ_1 and Γ_2 are empirical coefficients for including the effects of turbulent diffusion and a non-uniform air concentration distribution. In this equation, the parameters averaged over the depth are denoted by an overbar. The equation for the bubble rise velocity in a non-hydrostatic flow condition (Rutschmann et al., 1986) is simplified by setting $\rho_a/\rho_w\cong 0$, as in Chanson (2013). Using Equation (7) in the derived expression results in

$$\overline{w}_B^2\cong w_{B0}^2\left(\frac{|\rho_w gH+p_D|}{\rho_w gH}\right), \tag{15}$$

where w_{B0} is the rising velocity of a bubble in still water and can be determined by using empirical equations and/or design charts (see Haberman and Morton, 1953; Comolet, 1979). For an air-water flow with a streamwise velocity, the effect of a bubble cloud on the bubble rise velocity of a solitary bubble is likely insignificant (Kobus, 1991); thus, it is ignored here.

2.3.2 Flux of entrained air

The source term in Equation (14), which pertains to air entrainment occurring at the free surface, can be estimated by the following equations (Hirt, 2003; Souders and Hirt, 2004):

$$\overline{R}_s=\frac{K_a}{\Delta H}\left(\frac{2(E_t-E_d)}{\rho}\right)^{1/2}, \tag{16a}$$

$$E_t=\rho\overline{k}, \tag{16b}$$

$$E_d=\rho g_n L_t+\frac{\sigma_s}{L_t}, \tag{16c}$$

$$L_t=C_l\left(\frac{3}{2}\frac{\overline{k}^3}{\overline{\varepsilon}^2}\right)^{1/2}, \tag{16d}$$

where L_t is the turbulent length scale; E_t is the turbulent energy; E_d is the energy of gravity and surface tension; σ_s is the surface tension; $C_l = 0.0845$; K_a is a proportionality coefficient; and g_n is the normal component of the gravitational acceleration at the free surface. The evaluation of the above equations requires the estimation of the turbulence parameters and the mean air concentration. When the critical condition $E_t > E_d$ is met, air is drawn into the flow at the free surface. Following the Ma et al. (2011) approach, the entrained air is dispersed as a volumetric source within a layer of thickness ΔH located near the rough free surface where the air cavities are generated. The value of ΔH can be estimated by considering some characteristic length scale of the flow problem.

When air is entrained, the air concentration at the air-water interface must be equal to 90%. If it exceeds this limit, then the process of deaeration will be implemented by applying a constraint on the source term as follows:

$$\overline{R}_s = \min\left(\frac{K_a}{\Delta H}\left(\frac{2(E_t - E_d)}{\rho}\right)^{1/2}, \Gamma_L\right), \tag{17a}$$

$$\Gamma_L \cong \frac{\overline{C}_{\max} - C_{m*}}{\Delta t}, \tag{17b}$$

where $\overline{C}_{\max}$ is the maximum value of the mean air concentration which can be estimated from the results of the experimental investigations, and C_{m*} is the mean air concentration at the preceding time level. The above procedure regulates the air concentration at the air-water interface.

3. NUMERICAL SCHEME

Numerical solutions for the governing equations are obtained by using a hybrid numerical scheme that employs the finite-volume and finite-difference methods. The scheme applies the finite-volume method to the conservative form of the equations, and the derivatives in the source terms are discretized by the finite-difference equations. The following sections will outline the key steps involved in the development of the scheme, namely the procedure for calculating flux, the predictor-corrector approach for time stepping, and the implicit numerical technique. For additional information concerning the numerical scheme, see Zerihun (2024).

3.1 Numerical flux computation

The governing equations of this study may be written in a vector form as

$$\frac{\partial U}{\partial t} + \frac{\partial F(U)}{\partial x} = S, \tag{18}$$

where U, $F(U)$, and S are vectors of the unknown conserved variables, fluxes, and source terms, respectively, and are given by

$$U = \begin{pmatrix} H \\ q\rho \\ q\rho\left(\beta_4 \dfrac{\partial H}{\partial x}\right) \\ \rho H \bar{k} \\ \rho H \bar{\varepsilon} \\ HC_m \end{pmatrix}, \tag{19a}$$

$$F(U) = \begin{pmatrix} q \\ \rho\left(\beta_1 \dfrac{q^2}{H} + \dfrac{gH^2}{2}\right) \\ \dfrac{\rho q^2}{H}\left(\beta_2 \dfrac{\partial H}{\partial x} + \beta_1 \dfrac{\partial Z}{\partial x}\right) \\ \rho q \bar{k} \\ \rho q \bar{\varepsilon} \\ qC_m \end{pmatrix}, \tag{19b}$$

$$S = \begin{pmatrix} -\dfrac{1}{\rho}\left(H \dfrac{\partial \rho}{\partial t} + q \dfrac{\partial \rho}{\partial x}\right) \\ -\left(\rho g H + p_D\right)\dfrac{\partial Z}{\partial x} - \dfrac{\partial}{\partial x}\left(\dfrac{Hp_D}{2}\right) + \dfrac{\partial}{\partial x}\left(H\bar{\sigma}_x\right) - \tau_b \\ p_D - \tau_b \dfrac{\partial Z}{\partial x} + \dfrac{\partial}{\partial x}\left(H\bar{\tau}_{zx}\right) + \Psi_L \\ \dfrac{\partial}{\partial x}\left(H\left(\mu + \dfrac{\bar{\xi}}{\sigma_k}\right)\dfrac{\partial \bar{k}}{\partial x}\right) + \rho H\left(P_{k\xi} + P_H \dfrac{\bar{k}^2}{\bar{\varepsilon}} - \bar{\varepsilon}\right) \\ \dfrac{\partial}{\partial x}\left(H\left(\mu + \dfrac{\bar{\xi}}{\sigma_\varepsilon}\right)\dfrac{\partial \bar{\varepsilon}}{\partial x}\right) + \rho H\left(P_{\varepsilon\xi} + C_{1\varepsilon} P_H \bar{k} - C_{2\varepsilon}\dfrac{\bar{\varepsilon}^2}{\bar{k}}\right) \\ \xi_a \dfrac{\Gamma_2 C_m}{H} + H\bar{R}_s - \Gamma_1 \bar{w}_B C_m \end{pmatrix}, \tag{19c}$$

$$\Psi_L = \beta_3 \frac{\partial}{\partial t}\left(H\rho \frac{\partial q}{\partial x} - qH \frac{\partial \rho}{\partial x}\right) + \frac{q}{2}\left(\rho \frac{\partial^2 q}{\partial x^2} + q \frac{\partial^2 \rho}{\partial x^2}\right) + \frac{qH}{2}\frac{\partial}{\partial t}\left(\frac{\partial \rho}{\partial x}\right). \tag{19d}$$

Integrating Equation (18) over a control volume in the $x-t$ plane (Hirsch, 2007, p. 208) and discretizing the resulting expression using Euler's time-stepping scheme yields the following equation:

$$U_i^{N+1} = U_i^N - \frac{\Delta t}{\Delta x}\left(F(U)_{i+1/2}^N - F(U)_{i-1/2}^N\right) + \Delta t S_i^N, \tag{20}$$

where Δx is the spatial step size in the x-direction; i is a computational point index; Δt is the time step; N stands for the current time level; and $F(U)_{i\pm1/2}$ are the numerical fluxes through the cell interfaces at $i-1/2$ and $i+1/2$. For the purpose of obtaining data relevant to the multi-step time integration scheme at the time levels 1 and 2, Equation (20) is solved numerically by explicit and implicit methods.

Before estimating the numerical fluxes, the conserved variables on the cell interfaces are reconstructed using the total variation-diminishing version of a fourth-order monotone upstream-centered scheme for the conservation laws (MUSCL-TVD), which was introduced by Yamamoto and Daiguji (1993). In the scheme, two-step limiter functions are adopted to suppress numerical oscillations and maintain monotonicity near shocks. Moreover, the weighted surface-depth gradient method (Aureli et al., 2008) is applied to compute the flow depths at the cell interfaces, averting the prevalence of numerical instability due to a discontinuous bed profile or steep bed gradient. This method computes a weighted mean of the values derived from the depth-gradient and surface-gradient methods and overcomes the limitations of these methods. The Harten-Lax-van Leer (HLL) approximate Riemann solver (Harten et al., 1983) is also applied to compute the numerical fluxes at the cell interfaces using the reconstructed values from the neighboring cells. As suggested by LeVeque (2004, pp. 129-130), ghost cells at the upstream and downstream ends of the computational domain are incorporated to obtain complete solutions for the unknown variables. Using an extrapolation method, the values of the variables at these cells are estimated from the interior cell values.

3.2 Time integration and solution methods

The time integration process is carried out in two steps utilizing a finite-difference predictor-corrector scheme (Bashforth and Adams, 1883). In the predictor step, the time derivative term in Equation (18) is discretized using the third-order accurate scheme. The resulting equation can be expressed as

$$U_i^P = U_i^N + \frac{\Delta t}{12}\left(23\Omega_i^N - 16\Omega_i^{N-1} + 5\Omega_i^{N-2}\right), \tag{21a}$$

$$\Omega_i = -\frac{1}{\Delta x}\left(F(U)_{i+1/2} - F(U)_{i-1/2}\right) + S_i, \tag{21b}$$

where index P refers to the predictor step, and the superscripts $N-1$ and $N-2$ denote the previous time levels. In this step, Ω_i is determined by employing the known values of the variables in Equation (21b).

In the corrector step, the time integration is carried out by applying the fourth-order Adams–Moulton scheme with the predicted and known cell-averaged values. Using the scheme originally proposed by Adams (Bashforth and Adams, 1883), Equation (18) is discretized to yield

$$U_i^C = U_i^N + \frac{\Delta t}{24}\left(9\Omega_i^P + 19\Omega_i^N - 5\Omega_i^{N-1} + \Omega_i^{N-2}\right), \tag{21c}$$

where index C stands for the corrector step. Likewise, Ω_i^P is evaluated using the values of the conserved variables from the predictor step. Because of their weak non-linear coefficients, the equations of continuity, air transport, and turbulence model are solved explicitly at all the time levels. For accuracy and numerical stability purposes, however, the depth-averaged momentum equations are solved implicitly for the unknown variables q and p_D at the predictor and corrector steps. Using Equations (21a) and (21c) and the finite-difference equations (Bickley, 1941) for the derivatives in the source terms, these dynamic equations are discretized in both steps of the computation. The various terms of the resulting equations are evaluated using the known values of the conserved variables from the previous time levels. This results in a system of non-linear algebraic equations, which can be expressed in a general form by

$$\varphi_{1,i} q_i^{N+1} + \varphi_{2,i+1} p_{D,i+1}^N + \varphi_{3,i} p_{D,i}^N + \varphi_{4,i-1} p_{D,i-1}^N = \varphi_5, \quad (22)$$

where $\varphi_1, \varphi_2, ..., \varphi_5$ are the coefficients of the discretized equations. Such implicit sets of equations, along with the implemented boundary conditions, were iteratively solved at both steps of the computation. The equations are first reduced to a linear form by the Newton–Raphson method with numerical Jacobian matrices and then solved using the direct solution method of LU decomposition, as was previously done by Zerihun (2017a, 2019). The final results of the applications of the explicit and implicit methods are the cell-averaged values of the conserved variables at different time levels.

4. MODEL VALIDATION AND DISCUSSION

4.1 Test cases and experimental data

In the next sections, the feasibility of the proposed model is examined by simulating two different types of self-aerated flows in open channels. These are: (i) a free hydraulic jump with a non-aerated approach flow; and (ii) a turbulent flow over a smooth (planar bed) spillway chute. Such steady, open-channel flow problems were solved herein as unsteady flow problems by using time as an iterative parameter until the steady-state solutions were achieved. The convergence of the solutions of the numerical model was rigorously examined for various values of spatial step size and time step. For accurately modeling the local flow characteristics of the problems, a step size, which is smaller than 25% of the flow depth at the upstream end section, was employed. For step size coarser than this threshold value, the results were in less agreement with the experimental data. Additionally, a numerical stability criterion based on the Courant–Friedrichs–Lewy (CFL) condition was applied to control the time step size, with a CFL value between 0.1 and 0.45 to achieve stable and reliable results.

An extensive dataset of experimental results was sourced from the literature to calibrate and assess the model's performance. The experiments were conducted in the laboratory flumes for discharges between 35.8 and 630 L/s/m and covered various experimental conditions, with inflow Froude numbers varying from 3.8 to 15.5 and approaching Reynolds numbers ranging from 0.35×10^5 to 370×10^5. Besides, field data (Wood et al., 1983) were employed to corroborate some of the numerical results. The chosen data were devoid of size-scale influences attributed to surface tension and viscosity.

4.2 Boundary and initial conditions

The numerical solutions of the mixture flow problems using the preceding governing equations require the specification of six external boundary conditions. These conditions can be imposed solely at the inflow section or at both the inflow and outflow sections. For all test cases, the flow depth, discharge, mean air concentration, and dynamic bed pressure were specified at the inflow section. In addition, the turbulence variables ($\bar{k}$ and $\bar{\varepsilon}$) at this section were approximated for a rough estimate of the eddy viscosity (Ferziger and Peric, 2002, p. 300). Only for the hydraulic jump test case, a constant subcritical flow depth was imposed at the outflow section to allow the jump to take place. The prescribed boundary values remained unaltered throughout the numerical computations. The flow at $t=0$ s was assumed to be a supercritical uniform flow ($p_D=0$) with a flow depth equal to the boundary inflow value. For the case of an initial dry-bed condition, a flow depth of 1 mm was set to avoid undesirable numerical instability.

4.3 Free hydraulic jump

The free hydraulic jump is a transitional open-channel flow from a supercritical to a subcritical state. It is distinguished by a rapid rise in free-surface elevation and is usually accompanied by strong turbulence and air entrainment. The model's ability for accurately simulating these characteristics is examined here by treating the jump as a 2D vertical plane flow. The results of the model for the mean free-surface profile along the centerline of the channel were compared with various experimental datasets (Schröder, 1963; Hager, 1993; Wang, 2014). Figure 3a shows the normalized free-surface profiles $\Phi\,(=(H-H_1)/(H_2-H_1)$, where H_1 and H_2 are the sequent depths at the upstream and downstream ends of the jump, respectively) versus the normalized horizontal distance $\mathrm{X}\,(=x/L_R$, where L_R is the length of the roller) for free jumps with the approaching Froude numbers (F_{r0}) varying from 3.8 to 8.5. The profiles exhibit self-similarity, as previously noted by Schröder (1963). It is evident that the jump roller length and the key characteristics of the free-surface profile were predicted reasonably well by the model. The predicted profile for $F_{r0}=7.5$ shows a monotonically rising free-surface level, and its slope changes from a steep to a mild near the end of the roller flow zone. In the supercritical flow region near the toe of the jump, however, the elevation of the free surface was slightly overestimated. This is probably due to the minor difference between the experimental and numerical results for the mean location of the toe of the jump. A short distance further downstream, the correlation between the numerical results and the experimental data was deemed satisfactory, demonstrating the model's capacity for handling the effects of streamline curvature and two-phase flow features. As depicted in Figure 3b, the computed mean air concentration favorably agreed with the measurements and followed the general trend of the observed data.

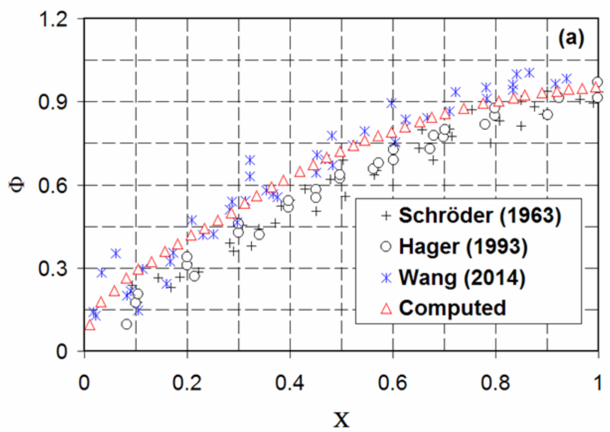

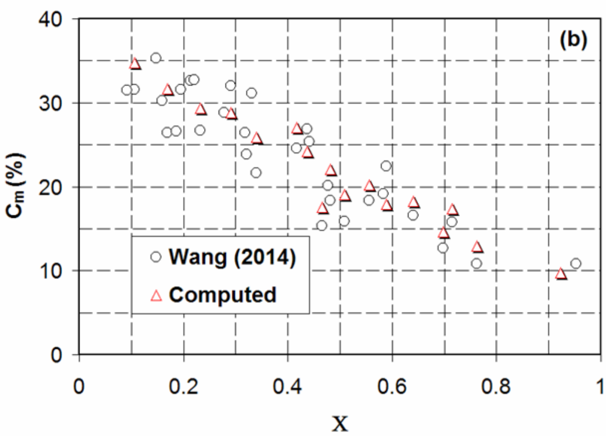

Figure 3. (a) Non-dimensional free-surface profile; and (b) streamwise variation of the mean air concentration $C_m(X)$ for the considered range of F_{r0} values.

Similar to the previous test case, the free-surface elevation of the free hydraulic jump with $F_{r0}=5.1$ was satisfactorily predicted by the model, as shown in Figure 4a. Furthermore, its pressure distributions at various sections downstream of the toe of the jump are depicted in Figure

4b. In this figure, the non-dimensional pressure, $p/\gamma_w H_1$, is plotted as a function of z/H_1; where γ_w is the unit weight of water. With an increase in distance from the toe of the jump, the significance of the effects of streamline curvature and air concentration diminishes. It is evident from Figure 4b that for this flow situation, the bottom pressure varies from 70 to 85% of the corresponding static pressure. As expected, the results demonstrate the strong dependence of the pressure field on the dynamic effects of the air-water mixture flow for a jump with $F_{r0} > 5$. This conclusion is in agreement with that of McCorquodale and Khalifa (1983).

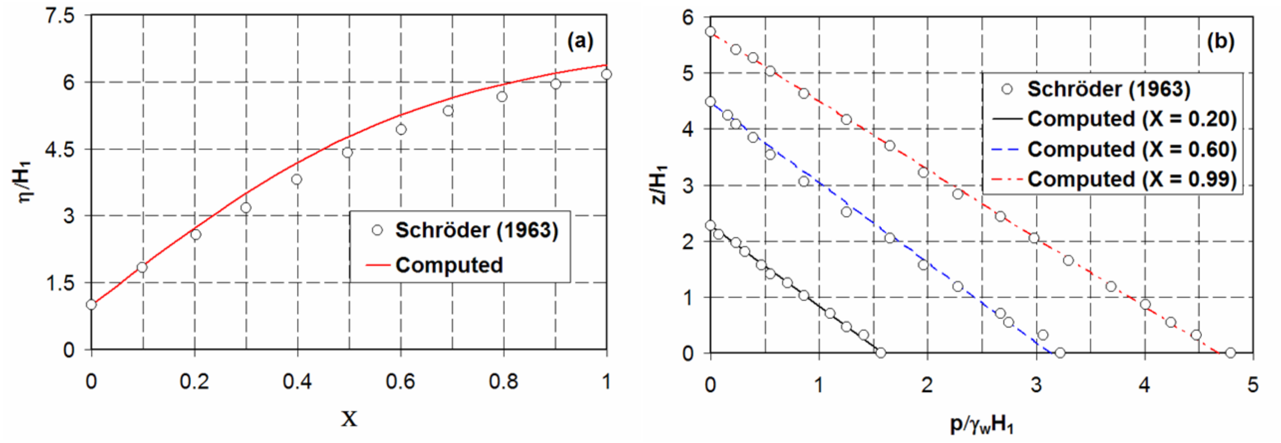

Figure 4. Comparison of the free-surface and pressure profiles of a free hydraulic jump with the experimental data of Schröder (1963) for $q = 241$ L/s/m. The pressure distributions at various sections are shown in (b).

4.4 Turbulent rough flow along a smooth spillway chute

Self-aerated open-channel flow along the spillway chute is divided into three distinct regions. According to Wood (1983), these regions are a non-aerated approach zone, a gradually-varied aerated flow zone, and a uniform aerated flow zone (illustrated in Figure 5). The tasks of modeling this flow involve identification of the point of incipient aeration and simulation of the aerated flow in the zones immediately downstream of this point. The preceding model, which was formulated for fully developed turbulent flow, is not applicable to analyze flow in non-aerated zone. By applying the momentum principle in the main flow and boundary-layer regions, this developing turbulent flow was previously investigated by Iwasa (1957). He also verified the numerical results by comparing them with the experimental data related to this type of flow in a hydraulically smooth channel. In this study, an accurate module is developed to simulate both the free-surface and boundary-layer profiles and is integrated with the proposed model. In practice, these profiles are used to determine the location of the inception point of free-surface aeration (Lane, 1939; Bauer, 1951).

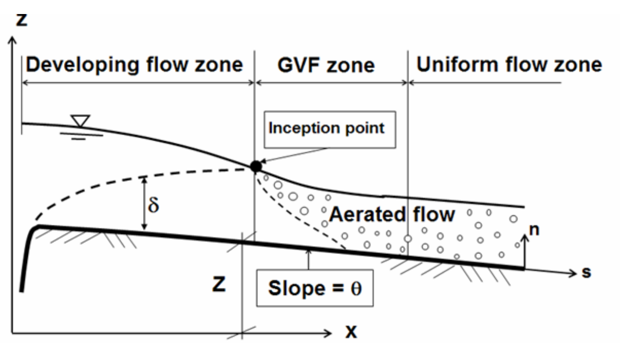

Figure 5. Flow regions along the spillway chute. GVF refers to gradually-varied flow for an aerated open-channel flow.

4.4.1 Location of incipient aeration

In a developing turbulent flow problem, the free-surface profile is computed by taking into account the boundary-layer development. For this non-aerated flow problem, the flow profile equation, which comprises the flow depth and the boundary-layer displacement thickness, was derived here by vertically integrating the momentum equation in the x-direction (for details, see the Appendix). The resulting equation reads:

$$\left(1-\frac{q^2}{g\cos^2\theta\left(H-\delta^*\right)^3}\right)\frac{dH}{dx}+\left(\frac{q^2}{g\cos^2\theta\left(H-\delta^*\right)^3}\right)\frac{d\delta^*}{dx}+\frac{dZ}{dx}=0, \qquad (23)$$

where θ is the chute slope, and δ^* stands for the boundary-layer displacement thickness whose value is not very sensitive to the choice of velocity distribution profile (Montes, 1998, p. 600). Using the momentum principle (Iwasa, 1957) and potential-flow approach (Silberman, 1980), they previously proposed an equation structurally similar to this equation. The complete numerical solution of Equation (23) requires two additional closure relations. Using the wall-wake law for the velocity profile in the turbulent boundary layer, the approximate expression for the displacement thickness is (White, 1991, p. 420)

$$\frac{\delta^*}{\delta}=\frac{1+\Pi}{KU_e/U_\tau}, \qquad (24)$$

where Π is the Coles wake parameter whose value can be estimated by analyzing velocity data or by using an empirical equation (Kironoto and Graf, 1995); U_e is the velocity at the edge of the boundary layer; and δ is the boundary-layer thickness. For chute slopes varying between 20 and 60º, the profile of this layer can be determined by the following empirical equation:

$$\frac{Y}{\chi}=0.053\left(\frac{\chi}{\vartheta}\right)^{-0.21}, \qquad (25)$$

where $Y\left(=\delta\cos\theta/H_c\right)$ is the relative boundary-layer thickness normal to the bed; H_c is the critical flow depth; $\vartheta\left(=k_s/H_c\right)$ is the relative equivalent roughness height; k_s is the equivalent roughness height; and $\chi\left(=s/H_c\right)$ is a non-dimensional distance along the chute bed. The above equation was the result of analyzing a set of measured data (Hickox, 1945; Bauer, 1951; Bormann, 1968) using a non-linear optimization approach. As previously noted (see, e.g., Halbronn, 1955; Campbell et al., 1965), the k_s value of the screen-roughened surface estimated by Bauer was unexpectedly high. After re-analyzing the Bauer data, a k_s value of 0.74 mm was obtained and used for developing Equation (25). This value was favorably agreed with the result of earlier investigation (Furuya and Fujita, 1967) for a similar bed roughness configuration. Figure 6 shows the result of the calibration, with a coefficient of determination $R^2=0.89$. It also compares the present result with the field data of Wood et al. (1983), resulting in a satisfactory agreement. Equations (23)-(25) are coupled, and the resulting expression is solved numerically with fourth-order Hamming's method (Carnahan et al., 1990, pp. 390-392) by specifying a flow depth as a boundary condition at the inflow section.

Figure 7 compares the computed relative boundary-layer and flow depth profiles with the experimental data (Bauer, 1951; Bormann, 1968). It is worth noting that the experimental data for the relative flow depths normal to the bed, $\Psi\left(=H\cos\theta/H_c\right)$, are reckoned from the measured velocity profiles and boundary-layer displacement thicknesses. For both profiles, the numerical results display a good correlation with the experimental data, with mean absolute relative errors

(MARE) of less than 5%. It is evident from Figures 7 and 8 that increasing the steepness of the chute slope shifts the point of incipient aeration further upstream toward the inflow section. A similar trend is also observed for the effect of relative roughness on the location of this point, in agreement with that of Keller and Rastogi (1975).

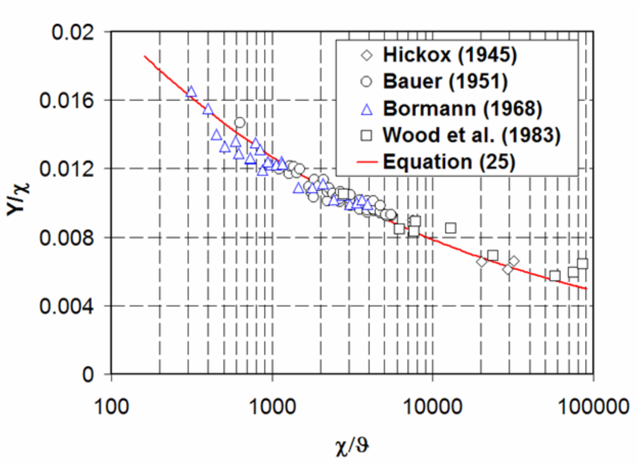

Figure 6. Comparison of predicted and measured relative boundary-layer thickness for open-channel flows over rough boundaries.

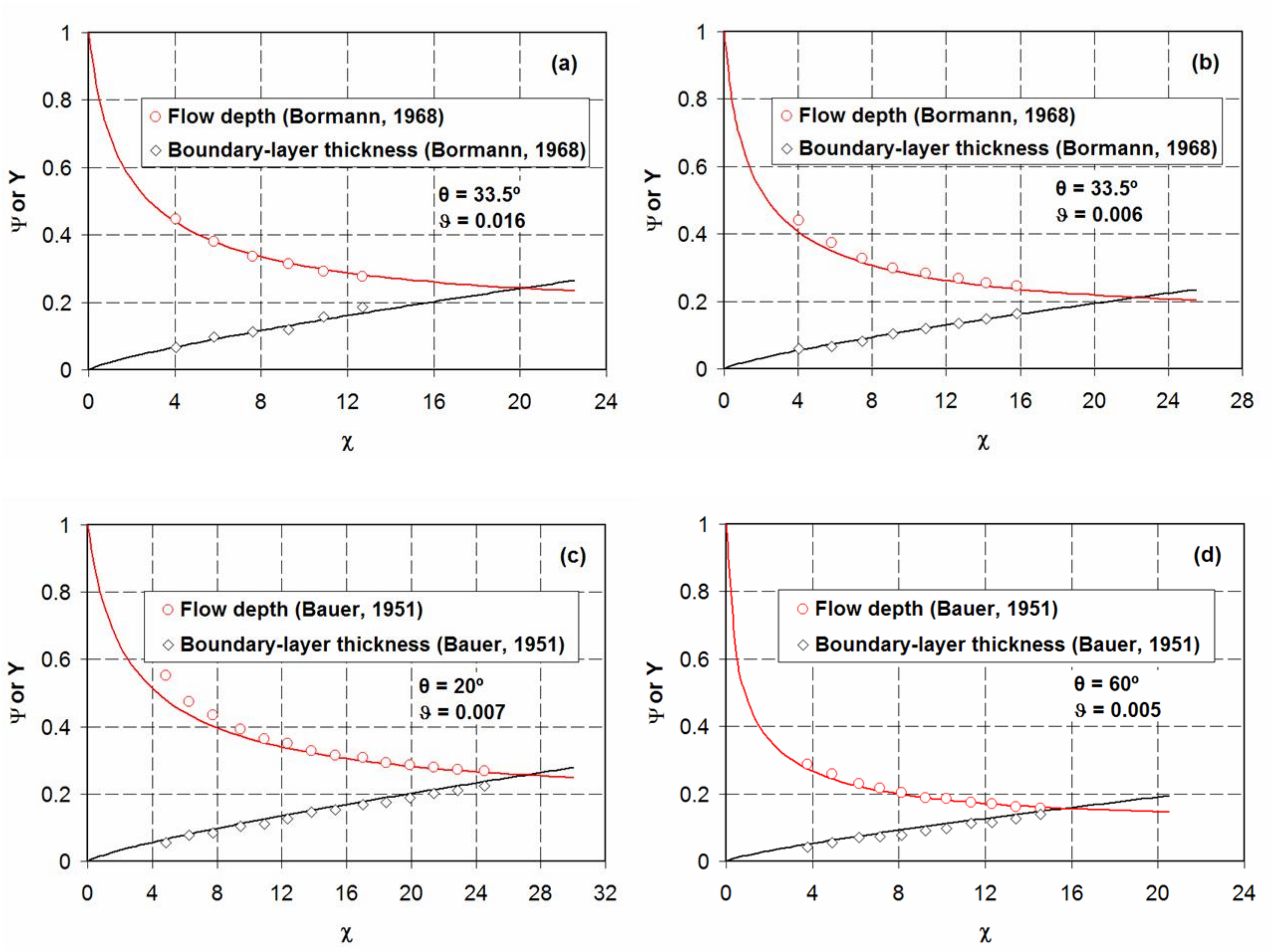

Figure 7. Relative flow depth and boundary-layer profiles for hypercritical open-channel flows over spillway chutes. The results obtained from the computations are depicted by solid lines that correspond in color to the experimental data.

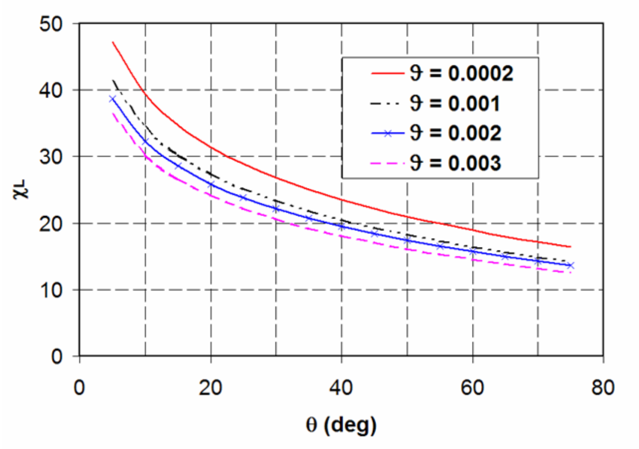

Figure 8. The location of incipient aeration χ_L as a function of the chute slope for various values of relative roughness ϑ.

4.4.2 Self-aerated chute flow

The model's predictive capability was investigated by simulating the mean air concentration of a hypercritical flow ($F_{r0} > 3$) in the aerated flow zone. Its results were compared with the experimental data obtained by Straub and Anderson (1960) and Killen (1968) and are depicted in Figure 9. For the aerated flows in mildly and steeply sloping chutes, the model results satisfactorily agreed with the measurements (MARE = 6.1%), as shown in Figure 9a. A minor difference between the numerical and experimental results can be observed for chutes steeper than 50º. The results demonstrated that the air entrainment capacity of the flow increases as the slope of the chute increases. This is due to the fact that the dynamic behavior of the hypercritical flow is predominantly influenced by the steepness of the streamline slope (Zerihun, 2016, 2017b).

The variation of the computed mean air concentration along the streamwise direction for a typical chute flow is presented in Figure 9b. The result revealed a gradual increase in mean air concentration within the GVF aerated flow region, ultimately approaching an equilibrium concentration. This trend was adequately simulated by the proposed model with a MARE of 7.7%. For the self-aerated flow problems considered, the overall performance of the numerical model was reasonably well.

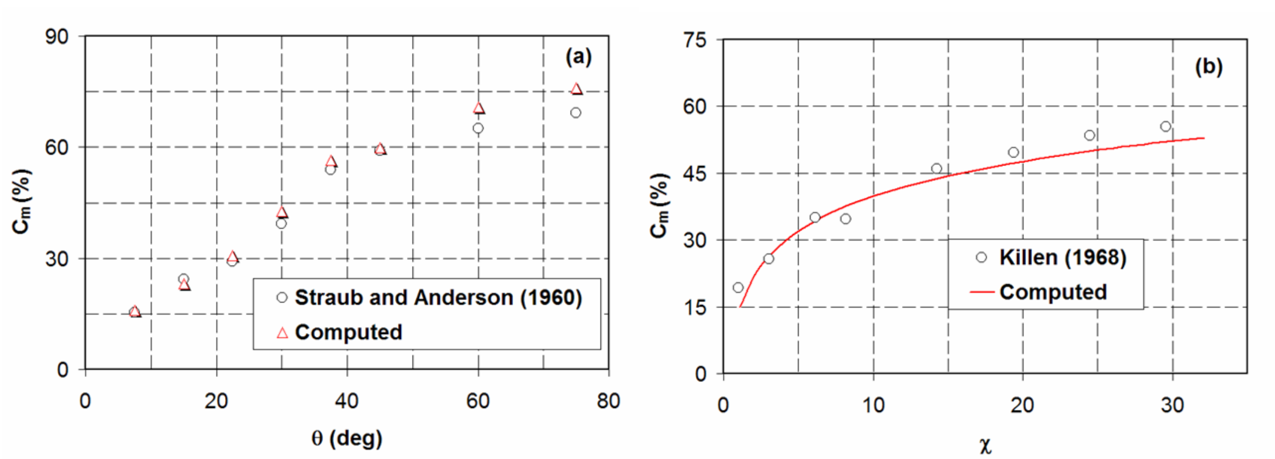

Figure 9. (a) Variation of the mean equilibrium air concentration with the chute slope θ ($q = 322.1$ L/s/m); and (b) mean air concentration versus non-dimensional distance from point of inception for a hypercritical flow over a chute with a 52.5º slope ($q = 399.5$ L/s/m).

5. CONCLUSIONS

A mixture flow model, which considers the effects of streamline curvature, steep gradient and air entrainment, was developed and then applied to investigate the mean flow characteristics of the self-aerated open-channel flows. The proposed model includes a coupled set of depth-averaged Boussinesq-type and air transport equations, and it is complemented by empirical relations derived from laboratory and prototype data. The applied approach endows the model with the capability to analyze a wide range of flow problems, with computations that are much faster than those of 3D simulations. A hybrid scheme that integrates finite-volume and finite-difference methods was adopted to discretize and solve the non-linear governing equations. To examine the performance of the proposed model, two specific numerical tests were carried out, and the results were compared against the measured data.

For the free hydraulic jump, the numerical results exhibited a good correlation with the experimental data, except in the supercritical flow region close to the toe of the jump. In this region, the elevation of the free surface was slightly overestimated. Furthermore, the computed pressure distributions at various sections followed the general trend of the observed data, with the dynamic pressure at the bottom varying from 15 to 30% of the corresponding static pressure. Overall, the results of the comparison substantiated the credibility of the proposed model in effectively simulating such a type of self-aerated open-channel flow.

As a part of this study, a numerical method for a non-aerated, hypercritical chute flow was proposed for computing the relative flow depth and boundary-layer profiles. Its application is limited to chute slopes between 20 and 60º. The analysis of the comparison results highlighted the effectiveness of the proposed method in determining the location of incipient aeration. For the problems of self-aerated flows in mildly and steeply sloping chutes, the overall accuracy of the numerical model in predicting the mean air concentration was adequate. The results of this investigation attested that the dynamic behavior of the two-phase flow over the smooth chute was favorably captured. It is therefore concluded that a mixture flow model of this type may assist practicing engineers in developing or modifying the conceptual design of a smooth invert spillway chute.

APPENDIX: DYNAMIC EQUATION FOR DEVELOPING CHUTE FLOW

For a steady 2D open-channel flow, the momentum equation in the x-direction is

$$u\frac{\partial u}{\partial x}+w\frac{\partial u}{\partial z}=-\frac{1}{\rho}\frac{\partial p}{\partial x}+\frac{1}{\rho}\frac{\partial \tau_{xz}}{\partial z}, \tag{26}$$

where τ_{xz} is the shear stress. Considering the effects of a steep bottom slope, the pressure equation for a gradually-varied flow can be written as (Chow, 1959, p. 32)

$$\frac{p}{\rho g}=(\eta-z)\cos^2\theta. \tag{27}$$

For a constant bed slope, differentiating Equation (27) with respect to x gives the following expression for the pressure gradient:

$$\frac{1}{\rho}\frac{\partial p}{\partial x}=g\cos^2\theta\frac{\partial \eta}{\partial x}. \tag{28}$$

By vertically integrating the horizontal velocity, the following expression for the discharge of a steady flow is obtained:

$$q = \int_{Z}^{\eta} u dz = \int_{Z}^{\delta+Z} u dz + \int_{\delta+Z}^{\eta} u dz = \int_{Z}^{\delta+Z} u dz + U_e (H - \delta). \tag{29}$$

The expression for the boundary-layer displacement thickness (Bauer, 1951; Iwasa, 1957) can be written in a form as follows:

$$\delta^* = \int_{Z}^{\delta+Z} \left(1 - \frac{u}{U_e}\right) dz = \delta - \frac{1}{U_e} \int_{Z}^{\delta+Z} u dz. \tag{30}$$

Combing Equations (29) and (30) leads to

$$q = U_e \left(H - \delta^*\right). \tag{31}$$

Substituting Equation (28) into Equation (26) and then vertically integrating the resulting expression from $z = Z + \delta$ to $z = \eta$ yields the following equation after simplifying the result using Equation (31) and re-arranging the terms:

$$\left(1 - \frac{q^2}{g \cos^2 \theta \left(H - \delta^*\right)^3}\right) \frac{dH}{dx} + \left(\frac{q^2}{g \cos^2 \theta \left(H - \delta^*\right)^3}\right) \frac{d\delta^*}{dx} + \frac{dZ}{dx} = 0. \tag{32}$$

REFERENCES

Almeland, S. K., Mukha, T., and Bensow, R. E. (2021) An improved air entrainment model for stepped spillways, Appl. Math. Model., 100, 170–191.

Aureli, F., Maranzoni, A., Mignosa, P., and Ziveri, C. (2008) A weighted surface-depth gradient method for the numerical integration of the 2D shallow-water equations with topography, Adv. Water Resour., 31(7), 962–974.

Bashforth, F. and Adams, J. C. (1883) An Attempt to Test the Theories of Capillary Action by Comparing the Theoretical and Measured Forms of Drops of Fluid, with an Explanation of the Method of Integration Employed in Constructing the Tables which Give the Theoretical Forms of Such Drops, Cambridge University Press, Cambridge, UK, 18–19.

Bauer, W. J. (1951) The Development of the Turbulent Boundary Layer on Steep Slopes, Ph.D. Thesis, The University of Iowa, Iowa, IA, USA.

Bickley, W. G. (1941) Formulae for numerical differentiation, Math. Gaz., 25(263), 19–27.

Boes, R. M. and Hager, W. H. (2003a) Two-phase flow characteristics of stepped spillways, J. Hydraul. Eng., 129(9), 661–670.

Boes, R. M. and Hager, W. H. (2003b) Hydraulic design of stepped spillways, J. Hydraul. Eng., 129(9), 671–679.

Bormann, K. (1968) Der Abfluß in Schußrinnen unter Berücksichtigung der Luftaufnahme (Chute Flow Considering Air Entrainment), Bericht Nr. 13, Versuchsanstalt für Wasserbau, Oskar von Miller Institut, Technischen Hochschule München, München, Germany [in German].

Boussinesq, J. (1877) Essai Sur la Théorie des Eaux Courantes (Essay on the Theory of Water Flow), Mémoires Présentés par Divers Savants à l'Académie des Sciences, Paris, 23(1), 1–680 [in French].

Campbell, F. B., Cox, R. C., and Boyd, M. B. (1965) Boundary-layer development and spillway energy losses, J. Hydraul. Div., 91(HY3), 149–163.

Carnahan, B., Luther, H. A., and Wilkes, J. O. (1990) Applied Numerical Methods; Krieger Publishing Company: Malabar, FL, USA.

Castro, A. M., Li, J., and Carrica, P. M. (2016) A mechanistic model of bubble entrainment in turbulent free-surface flows, Int. J. Multiph. Flow, 86, 35–55.

Chanel, P. G. and Doering, J. C. (2008) Assessment of spillway modeling using computational fluid dynamics, Can. J. Civ. Eng., 35, 1481–1485.

Chanson, H. (1994) Drag reduction in open-channel flow by aeration and suspended load, J. Hydraul. Res., 32(1), 87–101.

Chanson, H. and Toombes, L. (2002) Air-water flows down stepped chutes: Turbulence and flow structure observations, Int. J. Multiph. Flow, 27(11), 1737–1761.

Chanson, H. (2013) Advective diffusion of air bubbles in turbulent water flows, In: Fluid Mechanics of Environmental Interfaces, Taylor and Francis, Leiden, The Netherlands, Gualtieri, C. and Mihailovic, D. T. (eds.), 2nd ed., Chapter 7, 181–219.

Chow, V. T. (1959) Open-Channel Hydraulics; McGraw-Hill: New York, NY, USA.
Comolet, R. (1979) Sur le Mouvement d'une bulle de gaz dans un liquide (Gas bubble motion in a liquid medium), La Houille Blanche, 65(1), 31–42 [in French].
Estrella, J., Wüthrich, D., and Chanson, H. (2022) Two-phase air-water flows in hydraulic jumps at low Froude number: Similarity, scale effects and the need for field observations, Exp. Therm. Fluid Sci., 130, 110486 https://doi.org/10.1016/j.expthermflusci.2021.110486.
Falvey, H. T. (1980) Air water Flow in Hydraulic Structures, Engineering Monograph No. 41, Water and Power Resources Service, Denver, CO, USA.
Felder, S. and Chanson, H. (2009) Turbulence, dynamic similarity and scale effects in high-velocity free-surface flows above a stepped chute, Exp. Fluids, 47, 1–18.
Ferziger, J. H. and Peric, M. (2002) Computational Methods for Fluid Dynamics, 3rd rev. ed., Springer-Verlag Berlin Heidelberg: New York, NY, USA.
Furuya, Y. and Fujita, H. (1967) Turbulent boundary layers on wire screen roughnesses, JSME, Bulletin, 10(37), 77–86.
Haberman, W. L. and Morton, R. K. (1953) An Experimental Investigation of the Drag and Shape of Air Bubbles Rising in Various Liquids, Report 802, Armed Services Technical Information Agency, Dayton, OH, USA.
Hager, W. H. (1991) Uniform aerated chute flow, J. Hydraul. Eng., 117(4), 528–533.
Hager, W. H. (1993) Classical hydraulic jump: Free-surface profile, Can. J. Civ. Eng., 20, 536–539.
Halbronn, G. (1955) Discussion of "Turbulent boundary layer on steep slopes" by Bauer, W., Proc. ASCE, 81(1), 606.1–606.7.
Hall, L. S. (1943) Open-channel flow at high velocities, Trans. ASCE, 108(1), 1393–1434.
Harten, A., Lax, P. D., and van Leer, B. (1983) On upstream differencing and Godunov-type scheme for hyperbolic conservation laws, SIAM Rev. Soc. Ind. Appl. Math., 25(1), 35–61.
Hickox, G. H. (1945) Air entrainment on spillway faces, ASCE, Civ. Eng., 15(12), 562–563.
Hirsch, C. (2007) Numerical Computation of Internal and External Flows: Vol. 1 Fundamentals of Computational Fluid Dynamics, 2nd ed., Elsevier: Oxford, UK.
Hirt, C. W. (2003) Modeling turbulent entrainment of air at a free surface, Technical Note 61 (FSI-03-TN61), Flow Science Incorporated, Santa Fe, NM, USA.
Ho, D. K. and Riddette, K. M. (2010) Application of computational fluid dynamics to evaluate hydraulic performance of spillways in Australia, Aust. J. Civ. Eng., 6(1), 81–103.
Hohermuth, B., Schmocker, L., Boes, R. M., and Vetsch, D. F. (2021) Numerical simulation of air entrainment in uniform chute flow, J. Hydraul. Res., 59(3), 378–391.
Ishii, M. and Hibiki, T. (2011) Thermo-Fluid Dynamics of Two-Phase Flow, 2nd ed., Springer Science and Business Media, LLC: New York, NY, USA.
Iwasa, Y. (1957) Boundary layer growth of open-channel flows on a smooth bed and its contribution to practical application to channel design, Memoirs of the Faculty of Engineering, Kyoto University, 19(3), 229–254.
Jevdjevich, V. and Levin, L. (1953) Entrainment of air in flowing water and technical problems connected with it, In: Proceedings of the 5th IAHR Congress, Minneapolis, MN, USA, 1-4 Sept., 439–454.
Jones, W. P. and Launder, B. (1972) The prediction of laminarization with a two-equation model of turbulence, Int. J. Heat Mass Transf., 15, 301–314.
Keller, R. J. and Rastogi, A. K. (1975) Prediction of flow development on spillways, J. Hydraul. Div., 101(HY9), 1171–1184.
Killen, J. M. (1968) The Surface Characteristics of Self-Aerated Flow in Steep Channels, Ph.D. Thesis, University of Minnesota, Minneapolis, MN, USA.
Kirkgoz, M. S., Akoz, M. S., and Oner, A. A. (2009) Numerical modeling of flow over a chute spillway, J. Hydraul. Res., 47(6), 790–797.
Kironoto, B. A. and Graf, W. H. (1995) Turbulence characteristics in rough non-uniform open-channel flow, Proc. Instn. Civ. Eng., Water, Maritime and Energy, 112(12), 336–348.
Kobus, H. (1991) Introduction to air-water flows, In: Air Entrainment in Free-Surface Flows, IAHR Hydraulic Structures Design Manual No. 4, Hydraulic Design Considerations, Wood, I. R. (ed.), Balkema, Rotterdam, The Netherlands, 1–28.
Kramer, K., Hager, W. H., and Minor, H.-E. (2006) Development of air concentration on chute spillways, J. Hydraul. Eng., 132(9), 908–915.
Lane, E. W. (1939) Entrainment of air in swiftly flowing water, ASCE, Civ. Eng., 9(2), 89–91.
LeVeque, R. J. (2004) Finite-Volume Methods for Hyperbolic Problems; Cambridge University Press: Cambridge, UK.
Lopes, P., Leandro, J., and Carvalho, R. F. (2017) Self-aeration modeling using a sub-grid volume of fluid model, Int. J. Nonlinear Sci. Numer. Simul., 18(7–8), 559–574.
Ma, J., Oberai, A. A., Drew, D. A., Lahey, R. T., and Hyman, M. C. (2011) A comprehensive sub-grid air entrainment model for RANS modeling of free-surface bubbly flows, J. Comput. Multiph. Flows, 3(1), 41–56.
McCorquodale, J. A. and Khalifa, A. (1983) Internal flow in hydraulic jumps, J. Hydraul. Eng., 109(5), 684–701.
Montes, J. S. (1998) Hydraulics of Open-Channel Flow; ASCE Press: Reston, VA, USA.
Morovati, K. and Eghbalzadeh, A. (2018) Study of inception point, void fraction and pressure over pooled stepped spillways using Flow-3D, Int. J. Numer. Methods Heat Fluid Flow, 28(4), 982–998.
Ohtsu, I., Yasuda, Y., and Takahashi, M. (2004) Flow characteristics of skimming flows in stepped channels, J. Hydraul. Eng., 130(9), 860–869.
Olsen, N. R. B. and Kjellesvig, H. M. (1998) Three-dimensional numerical flow modeling for estimation of spillway capacity, J. Hydraul. Res., 36(5), 775–784.
Pfister, M. and Hager, W. H. (2011) Self-entrainment of air on stepped spillways, Int. J. Multiph. Flow, 37(2), 99–107.
Rastogi, A. K. and Rodi, W. (1978) Prediction of heat and mass transfer in open channels, J. Hydraul. Div., 104(HY3), 397–420.

Rutschmann, P., Volkart, P., and Wood, I. R. (1986) Air entrainment at spillway aerators, In: Proceedings of the 9th Australasian Fluid Mechanics Conference, Auckland, New Zealand, 8–12 Dec., 350–353.

Schröder, R. (1963) Die turbulente Strömung im freien Wechselsprung: ein Beitrag zum Problem der luftdurchmischten Wasserströmung in offenen Gerinnen (The Turbulent Flow within the Free Hydraulic Jump: A Contribution to the Problem of Air-Water Flow in Open Channels), Habilitationsschrift, Institut für Wasserbau und Wasserwirtschaft, Technische Universität Berlin, Berlin, Germany [in German].

Silberman, E. (1980) Boundary layers in developing open-channel flow, J. Hydraul. Div., 106(HY7), 1237–1241.

Souders, D. T. and Hirt, C. W. (2004) Modeling entrainment of air at turbulent free surfaces, In: Proceedings of World Water and Environmental Resources Congress, Salt Lake City, UT, USA, 27 June–1 July, 1–10.

Straub, L. G. and Anderson, A. G. (1960) Self-aerated flow in open channels, Trans. ASCE, 125(1), 456–481.

Valero, D. and García-Bartual, R. (2016) Calibration of an air entrainment model for CFD spillway applications, In: Advances in Hydroinformatics, Gourbesville, P., Cunge, J., and Caignaert, G. (eds.), Springer Water, Singapore, https://doi.org/10.1007/978-981-287-615-7_38.

Wang, H. (2014) Turbulence and Air Entrainment in Hydraulic Jumps, Ph.D. Thesis, The University of Queensland, Brisbane, Qld, Australia.

White, F. M. (1991) Viscous Fluid Flow, 2nd ed., McGraw-Hill: New York, NY, USA.

Wilhelms, S. C. and Gulliver, J. S. (2005) Bubbles and waves description of self-aerated spillway flow, J. Hydraul. Res., 43(5), 522–531.

Wood, I. R. (1983) Uniform region of self-aerated flow, J. Hydraul. Eng., 109(3), 447–461.

Wood, I. R., Ackers, P., and Loveless, J. (1983) General method for critical point on spillways, J. Hydraul. Eng., 109(2), 308–312.

Yamamoto, S. and Daiguji, H. (1993) Higher-order accurate upwind schemes for solving the compressible Euler and Navier-Stokes equations, Comput. Fluids, 22(2–3), 259–270.

Yan, K. and Che, D. (2010) A coupled model for simulation of the gas-liquid two-phase flow with complex flow patterns, Int. J. Multiph. Flow, 36(4), 333–348.

Zabaleta, F., Márquez-Damián, S., and Bombardelli, F. A. (2023) A novel three-phase mixture approach for the numerical modeling of self-aerated flows, Comput. Methods Appl. Mech. Engrg., 408, https://doi.org/10.1016/j.cma.2023.115958.

Zerihun, Y. T. (2016) Modeling free-surface flow with curvilinear streamlines by a non-hydrostatic model, J. Hydrol. Hydromech., 64(3), 281–288.

Zerihun, Y. T. (2017a) A numerical study of non-hydrostatic shallow flows in open channels, Arch. Hydro-Eng. Environ. Mech., 64(1), 17–35.

Zerihun, Y. T. (2017b) A non-hydrostatic depth-averaged model for hydraulically steep free-surface flows, Fluids, 2(4), https://doi.org/10.3390/fluids2040049.

Zerihun, Y. T. (2019) On steady two-dimensional free-surface flows with spatially-varied discharges, Slovak J. Civ. Eng., 27(3), 1–11.

Zerihun, Y. T. (2021) Non-hydrostatic transitional open-channel flows from a supercritical to a subcritical state, Slovak J. Civ. Eng., 29(2), 39–48.

Zerihun, Y. T. (2024) Numerical modeling of sediment transport and bed evolution in nonuniform open-channel flows, Arch. Hydro-Eng. Environ. Mech., 71(1), 1–26.